minerals

MDPI

Article

A Novel Biomass-Derived Reductant for Nitric Acid Dissolution of Manganiferous Iron Ore: Comparative Assessment of Organic Reductants

Soner Top [1,*], Mahmut Altiner [2], Huseyin Vapur [2], Sait Kursunoglu [3,*] and Srecko Stopic [4]

[1] Department of Engineering Science, Abdullah Gul University, Kayseri 38080, Turkey
[2] Mining Engineering Department, Cukurova University, Adana 01330, Turkey; maltiner@cu.edu.tr (M.A.); hvapur@cu.edu.tr (H.V.)
[3] Department of Petroleum and Natural Gas Engineering, Batman University, Batman 72100, Turkey
[4] IME Process Metallurgy and Metal Recycling, RWTH Aachen University, Intzestrasse 3, 52068 Aachen, Germany
* Correspondence: soner.top@agu.edu.tr (S.T.); sait.kursunoglu@batman.edu.tr (S.K.)

Abstract

This study investigates the selective dissolution of manganese from a manganiferous iron ore using nitric acid (HNO_3) in the presence of various organic reductants. A series of leaching experiments was performed to evaluate the effects of temperature, reductant type, and leaching time on Mn recovery, with particular emphasis on biomass (horse dung) and tartaric acid as novel reducing agents. The dissolution behaviour of Fe, Mn, Mg, Ca, and Al was systematically examined, revealing that Mn extraction was strongly enhanced in the presence of reductants, while Fe dissolution remained below 10% under all conditions. The maximum Mn dissolution exceeded 90% at 90 °C using biomass and reached nearly 85%–90% with tartaric acid at elevated temperatures. Kinetic studies were conducted by applying reaction order models and the shrinking core model. The results indicated that Mn dissolution in HNO_3 medium is predominantly controlled by surface chemical reaction, with Arrhenius analysis yielding activation energies of 27.74 kJ/mol for biomass and 21.26 kJ/mol for tartaric acid. These relatively low values confirm the efficiency of organic reductants in facilitating Mn reduction and dissolution. To sum up, comparison of reductant efficiency revealed that, at the lowest concentrations, the dissolution of Mn followed the sequence glucose > sucrose > oxalic acid > tartaric acid > maleic acid > biomass > citric acid > acetic acid. At the highest concentrations, the trend shifted, with citric acid emerging as the most effective, followed by tartaric acid > oxalic acid > glucose > sucrose > maleic acid > biomass > acetic acid.

Keywords: manganiferous iron ores; manganese; iron; separation; dissolution

Academic Editor: Hyunjung Kim (Nick)

Received: 17 November 2025
Revised: 27 December 2025
Accepted: 30 December 2025
Published: 31 December 2025

1. Introduction

Iron is among the most abundant elements in the lithosphere, constituting nearly 5% of the Earth's crust. It primarily occurs in oxide minerals such as hematite (Fe_2O_3), magnetite (Fe_3O_4), and siderite ($FeCO_3$), as well as in sulfide minerals including pyrrhotite and pentlandite, particularly within igneous and metamorphic environments [1,2]. In contrast, manganese is significantly less common, representing about 0.095% of the crust and

ranking as the twelfth most abundant element. It almost exclusively occurs in mixed oxidation states, forming oxides, hydroxides, silicates, and carbonates, with pyrolusite (MnO_2) being the most widespread ore mineral [3,4].

Geologically, manganese is most often enriched in marine sedimentary environments, where it precipitates from seawater or groundwater to form deposits that greatly exceed its average crustal abundance [5]. Furthermore, manganese-rich oceanic nodules and crusts, composed of minerals such as vernadite, birnessite, and buserite, represent significant repositories of critical metals, including cobalt, nickel, and rare earth elements [6]. Iron, on the other hand, is extensively concentrated in banded iron formations (BIFs), which formed through chemical precipitation in Precambrian oceans. These deposits reflect alternating layers of iron oxides and silica, generated by redox fluctuations where Fe^{2+}-rich anoxic waters were episodically oxidized. Under certain geochemical conditions, manganese mineralization is also closely associated with these processes [7].

Due to their similar physicochemical characteristics and neighboring positions in the periodic table, manganese minerals such as pyrolusite were long misidentified as impure iron ores. Only with the advent of systematic chemical studies in the late eighteenth century, culminating in Gahn's isolation of metallic manganese in 1774, was manganese established as a distinct element [8].

Iron forms the foundation of modern infrastructure, with more than 90% of global metal production dedicated to steelmaking [9]. Its primary applications encompass construction, transportation, and energy sectors, including reinforced concrete, bridges, pipelines, ships, automobiles, railways, wind turbines, and power plants [10,11]. Beyond conventional steel, high-purity iron and advanced alloys are employed in electrical steels, magnetic materials, and biomedical devices, highlighting the element's versatility across industrial and technological domains. Manganese is equally indispensable as an alloying component, particularly in steelmaking, where it improves strength, wear resistance, and toughness while mitigating sulfur-induced embrittlement [12]. Approximately 85%–90% of global Mn consumption is attributed to ferroalloy production, with the remainder used in high-value applications such as Li-ion and alkaline batteries, pigments, fertilizers, catalysis, and advanced energy materials [13]. Consequently, manganese functions not only as a bulk metallurgical element but also as a critical material for emerging green technologies.

Conventional beneficiation techniques such as washing, gravity concentration, magnetic separation, and flotation have been widely applied to improve the grade of manganese and iron ores [14,15]. However, the complex mineralogy and fine intergrowth of Fe–Mn ores often limit the effectiveness of these methods, making selective and efficient separation difficult to achieve [16]. In recent years, the selective dissolution of manganese from Fe–Mn ores through reductive leaching has attracted significant attention. Iron remains in the ionic state below pH ≈ 3.5 but begins to precipitate at higher pH values. In contrast, manganese exhibits a greater tendency to dissolve under acidic to near-neutral conditions, yielding pale pink Mn^{2+} ions, and is classified among metals with a high affinity for reduction [17]. The redox potential for the Mn(IV) → Mn(II) transformation has been reported as 21.62 V vs. SHE at 15 °C and 16.28 V vs. SHE at 95 °C, corresponding to Eh values of 1.24 V vs. SHE and 1.19 V vs. SHE, respectively [18]. These values suggest that elevated temperature alone is insufficient for MnO_2 reduction; instead, electron donors with relatively low redox potentials must be employed to provide electrons in solution. Therefore, the conversion of higher-valence manganese species (Mn(III), Mn(IV)) into Mn(II) requires lower Eh conditions, achievable through reductive leaching in acidic media.

The reductive dissolution of MnO_2 under acidic conditions can be expressed as:

$$MnO_2 + 4H^+ + 2e^- \leftrightarrow Mn^{2+} + 2H_2O \quad (1)$$

Reductive leaching has been extensively employed to recover manganese from ferruginous manganese and manganiferous iron ores, utilizing a diverse array of reductants. Reported agents include sucrose [19], pyrite [20], methanol [21], sulfur dioxide [22], oxalic acid [23], sawdust [24], corn stalks [25], molasses [26], carbohydrates [27,28], corn cobs [29], hydrogen peroxide [30], waste tea leaves [31], calcium sulfide [32], formic acid [33], lignin [34], tannic acid [35], ascorbic acid [36], bamboo sawdust [37], and even unconventional sources such as biomass [38]. Through these approaches, manganese oxides are effectively reduced and solubilized into the leach solution.

Recent studies indicate that nitric acid offers several practical advantages over conventional sulfuric acid systems. Studies on metal-rich waste demonstrate that HNO_3 yields higher dissolution efficiencies and cleaner leachates compared with H_2SO_4, which often forms sulfate-rich byproducts that complicate recovery processes [39]. Similar trends are observed in mineral matrices where nitric acid promotes more controlled dissolution and avoids passivating phases that slow extraction [40]. These findings suggest that the nitrate medium can provide a more flexible and regeneration-compatible environment consistent with the objectives of the present work. Moreover, HNO_3 has also been successfully employed for the dissolution of manganese ores under reductive conditions, demonstrating its effectiveness for Mn recovery in different mineral systems [26,41–43].

The authors have previously investigated the selective dissolution of manganese from manganiferous iron ores using different acid systems, including sulfuric acid with biomass as a reductant [38] and hydrochloric acid for the synthesis of Mn_3O_4 nanoparticles via a leaching–precipitation–calcination route [44]. Building upon these studies, the present work addresses an important gap by systematically examining nitric acid as an alternative leaching medium. For the first time, various organic reductants are evaluated for the selective dissolution of manganese from Fe–Mn ores in HNO_3 solution. In particular, the use of tartaric acid and biomass as reductants in a nitric acid environment for manganese dissolution has not been previously reported, highlighting the novelty and significance of the proposed approach.

2. Experimental

2.1. Material

The manganiferous iron ore used in this study was sourced from the Dokuztekne Fe–Mn deposit in the Ceyhan district of Adana, Turkey. The mineralization occurs within altered spilitic volcanics and limestone, structurally modified by NW–SE–trending faults [45]. The deposit formed during the Cretaceous and was later reworked in the Oligocene–Miocene, producing stratiform Fe–Mn horizons associated with basaltic–andesitic volcanics. Major ore minerals include hematite, braunite, bixbyite, psilomelane, kutnahorite, and manganite, while calcite, quartz and chlorite constitute the main gangue phases. Mn micronodules up to 2 mm occur within laminated siliceous schists of the Isali Formation [46]. The ore body extends for approximately 1.2 to 1.5 km with thicknesses varying between 2 and 11 m. Approximately 300 kg of representative material was collected from outcrops and stockpiles within the licensed area operated by Sönmez Çimento A.Ş. and transported to laboratory for experimental studies.

All dissolution and chemical analyses were performed using analytical-grade reagents and deionized water. Analytical-grade H_2SO_4, HCl, HNO_3, Na_2CO_3, and NaOH (Merck) were employed for solution preparation and pH adjustment. Reductive leaching experiments utilized analytical-grade tartaric acid (Carlo Erba, Milan, Italy), oxalic acid (Merck, Darmstadt, Germany), citric acid (Merck, Darmstadt, Germany), glucose monohydrate (Merck, Darmstadt, Germany), sucrose (Isolab, Wertheim, Germany), maleic acid

(Aromel Kimya, Istanbul, Turkey), and acetic acid (Merck, Darmstadt, Germany) as reducing agents. Biomass reductant was supplied as horse manure obtained in a single 50 kg batch from the Ahmet Kılıççıoğlu Horse Farm (Malatya, Turkey). The material was oven-dried at 80 °C for 3 days, then milled under dry conditions in a laboratory-scale ball mill charged with 10 kg of grinding media. After dry sieving, particles smaller than 1 mm were collected and used directly in the leaching experiments.

2.2. Characterization Techniques

For the initial characterization of the material, powder samples were analyzed using a Minipal 4 Panalytical X-ray fluorescence (XRF) spectrometer. In addition, wet chemical analyses were performed by dissolving the material in aqua regia to validate the XRF results. After the leaching experiments, elemental concentrations in the leach solutions were primarily determined by atomic absorption spectroscopy (AAS) using PerkinElmer PinAAcle 900F (PerkinElmer, Waltham, MA, USA) and PinAAcle 900H instruments (PerkinElmer, Waltham, MA, USA). To ensure analytical accuracy and validate the AAS results, selected representative leach solutions were additionally analyzed by inductively coupled plasma mass spectrometry (ICP-MS) using a PerkinElmer NexION 2000 P system (PerkinElmer, Waltham, MA, USA). The results obtained by ICP-MS showed good agreement with the AAS measurements. Phase identification of the solid samples was carried out with a Bruker Discover D8 X-ray diffractometer (XRD) (Bruker AXS, Karlsruhe, Germany). XRD measurements were performed on powder samples in the 10–90° 2θ range with a step size of 0.02° over a total scan time of 15 min. The obtained diffractograms were evaluated using Diffrac.Suite Eva software (version 4.0) with the updated PDF-2 database for mineral identification. For comminution processes, a laboratory-scale jaw crusher and ball mill were employed. The particle size distributions of the ground samples were subsequently determined using a Malvern Panalytical Mastersizer 2000 laser particle size analyzer (Malvern Panalytical, Malvern, UK). For Fourier-transform infrared (FTIR) characterization, spectra of the biomass samples were recorded using a Thermo Scientific Nicolet iS10 FTIR spectrometer (Thermo Scientific, Waltham, MA, USA) in the 4000–400 cm^{-1} range to identify the functional groups present in the material. Additionally, the calorific value of the biomass was determined using an IKA C 200 calorimeter to evaluate its energy content prior to thermal or chemical processing.

2.3. Leaching Tests

Figure 1 illustrates the experimental reflux setup employed in this study. The schematic representation (Figure 1a) and the corresponding laboratory assembly (Figure 1b) consist of a round-bottom flask (1) equipped with a thermometer (2) placed on a magnetic stirrer–heating plate (3), connected to a vertical water-cooled condenser (4). The condenser is supplied with cooling water through the inlet (5) and outlet (6) connections to ensure efficient condensation of vapours and their return to the reaction flask. This configuration enables controlled heating under reflux conditions, preventing solvent loss while maintaining a stable reaction temperature throughout the leaching procedure.

Leaching experiments were performed in a 250 mL two-neck round-bottom flask fitted with a reflux condenser and thermometer, placed on an Mtops MS300HS heated magnetic stirrer (Mtops, Seoul, Republic of Korea). A 100 mL acidic solution of the desired molarity was heated to the target temperature before adding the ground ore sample at the specified solid/liquid ratio. For tests with a reductant, the reducing agent was introduced 5 min prior to ore addition. Each leach ran for 1 h under continuous stirring. The slurry was then filtered through Whatman No. 1 paper, the residue washed twice with deionized water, and the filtrate diluted to a known volume. All leaching experiments were conducted in triplicate, and the dissolution values presented in the figures represent mean

values with a standard deviation that did not exceed ±5% for any data point. Dissolved metal concentrations were determined primarily by atomic absorption spectroscopy, while inductively coupled plasma mass spectrometry (ICP-MS) was employed for validation of selected samples. Dissolution percentages were calculated using Equation (2).

$$\text{Dissolution}(\%) = \frac{C_{PLS} \times V}{C_{ORE} \times W} \times 100 \quad (2)$$

where D is the dissolution (%), C_{PLS} is the concentration of element in the PLS (mg/L), V is the final volume of the PLS (L), C_{ORE} is the initial concentration of element in the ore (mg/kg), and W is the amount of ore used in the leaching (kg).

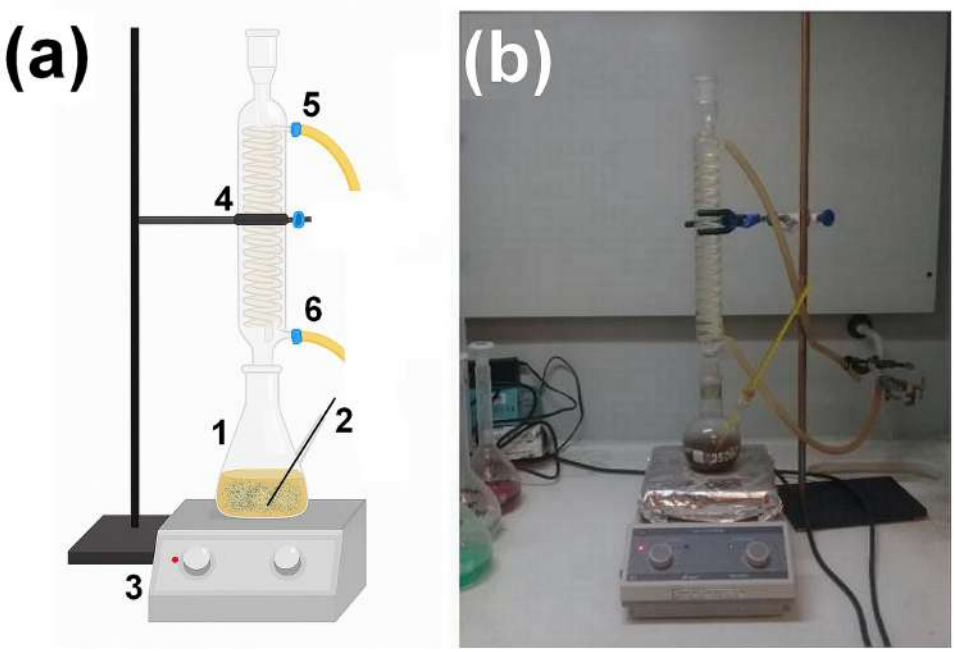

Figure 1. Experimental setup for the leaching process. (**a**) Schematic representation of the laboratory apparatus, showing the round-bottom flask (1) on a heating plate (3), thermometer (2), and vertical condenser (4) with water inlet (5) and outlet (6). (**b**) Photograph of the actual assembled system in the fume hood, illustrating the condenser cooling connections and heating arrangement.

3. Results and Discussion

3.1. Characterization

The chemical composition analysis of the manganiferous iron ore revealed that Fe_2O_3 (38.5%) and MnO (20.7%) are the predominant constituents, confirming the ore as a valuable source of both iron and manganese. The ore also contains considerable amounts of SiO_2 (14.91%) and CaO (5.82%), together with minor proportions of Al_2O_3 (3.10%) and MgO (1.62%). In addition, trace levels of PbO (0.24%), K_2O (0.24%), BaO (0.42%), SrO (0.36%), CuO (0.23%), TiO_2 (0.16%), NiO (0.12%), and SO_3 (0.18%) are present, along with very low concentrations of ZnO (0.06%), V_2O_5 (0.10%), ZrO_2 (0.04%), Ln_2O_3 (0.20%), and Re_2O_7 (0.05%). Overall, the ore exhibits a complex mineralogical composition, characterized by high iron and manganese contents accompanied by siliceous and calcareous gangue phases, as well as minor trace metal oxides. The XRD pattern of the manganese-bearing iron ore is presented in Figure 2. The analysis revealed that the ore consists of 69.7% crystalline and 30.3% amorphous phases. Within the crystalline fraction, 16.3% corresponds to hematite (PDF card no. 33-0664), 16.1% to goethite (PDF card no. 81-0464), 14.8% to manganite (PDF card no. 08-0099), 12.7% to maghemite (PDF card no. 39-1346),

12.5% to garnet (PDF card no. 03-0801), 9.2% to quartz (PDF card no. 46-1045), 8.3% to calcite (PDF card no. 05-0586), 7.8% to ramsdellite (PDF card no. 42-1316), and 2.2% to magnesium-bearing calcite (PDF card no. 86-2336).

The feed material was first crushed using a jaw crusher to reduce the particle size to below 1 cm. Subsequently, the sample was ground in a ball mill until the entire material passed below 200 μm (Figure 3a). The Hardgrove Grindability Index (HGI) of the feed was determined as 52.65, while the Bond work index was found to be 11.87 kWh/ton. Fine particle size is a critical parameter for enhancing the efficiency of leaching, as larger particles hinder the dissolution of mineral phases encapsulated within coarse grains. When leaching is performed on coarser fractions, the dissolution of enclosed minerals is restricted, leading to reduced extraction efficiency. For instance, Fe or Mn phases encapsulated within a quartz grain may not interact effectively with the leaching agent under the experimental conditions, or dissolution may only occur after prolonged exposure, following the dissolution of the surrounding mineral phase. Therefore, samples ground for 60 min to achieve a finer particle size distribution ($d_{50} \approx 11.5$ μm) were selected for subsequent leaching experiments (Figure 3b).

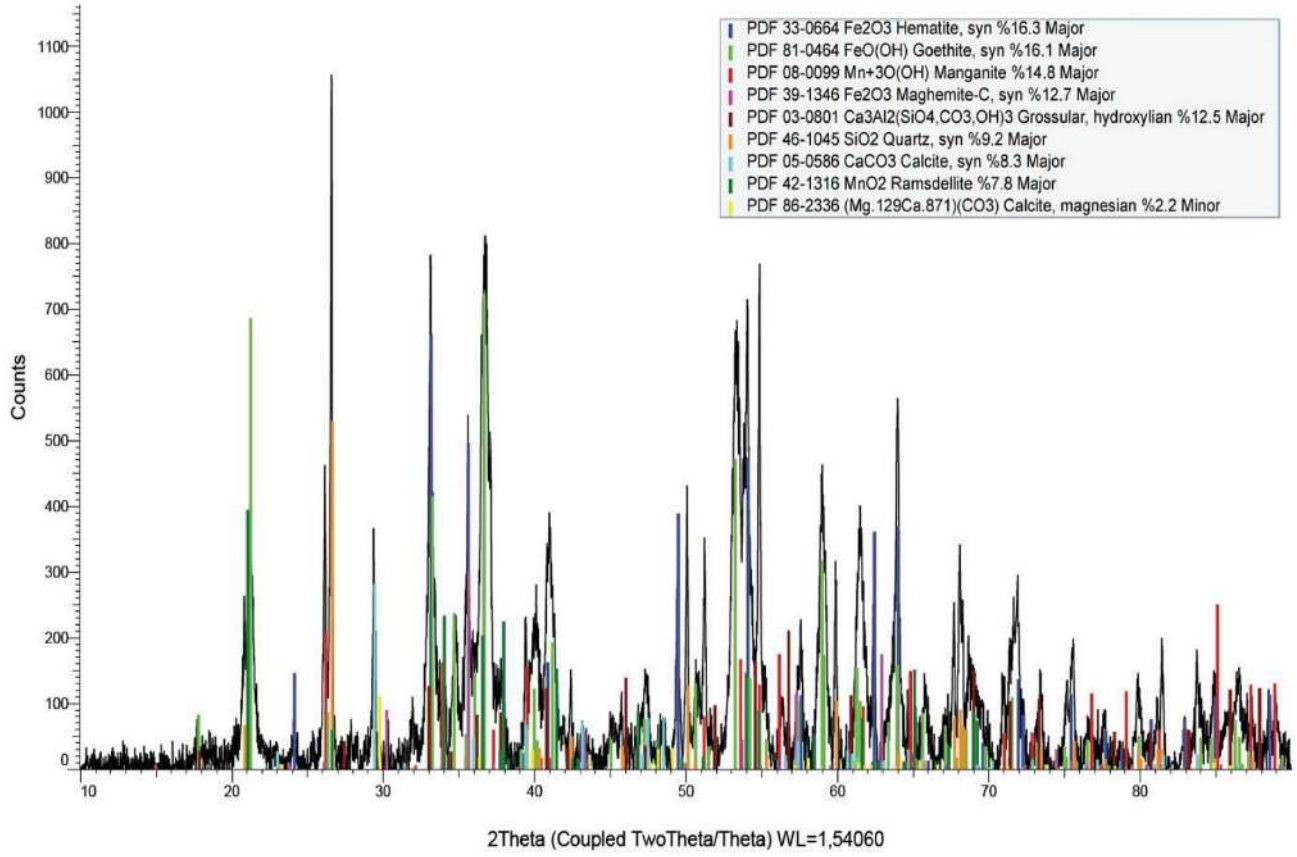

Figure 2. XRD pattern of manganiferous iron ore.

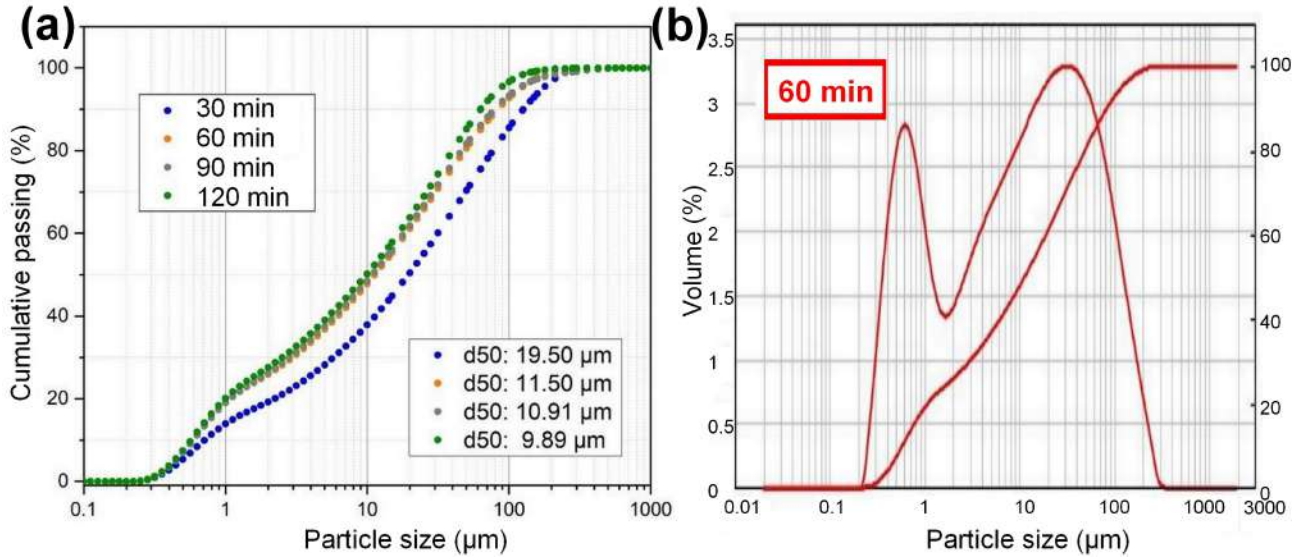

Figure 3. (**a**) Particle size distributions of the material ground for different milling durations. (**b**) Mastersizer particle size analysis of the sample after 1 h of milling.

To further elucidate the molecular structure and functional group composition of the biomass, FTIR analysis was performed (Figure 4). The region between 950 and 1200 cm^{-1} corresponds to functional groups associated with carbohydrates [47]. The main absorbance band was observed at 1036 cm^{-1}, indicating the presence of C–O bonds in the material. The peak at 1415 cm^{-1} represents asymmetric C–H and O–H vibrations as well as $–CH_2$ groups [48–50]. The peaks between 1632 and 1657 cm^{-1} are attributed to proteins and peptides [48,51]. The bands observed at 2850 and 2924 cm^{-1} are characteristic of fats and lipids. At lower frequencies, the peak at 3260 cm^{-1} arises from N–H stretching vibrations of proteins and O–H stretching associated with water and carbohydrates, whereas the peak at 2928 cm^{-1} mainly corresponds to the antisymmetric stretching of CH_2 methyl groups derived from lipids [47]. Overall, the FTIR results are consistent with previously reported characteristics of sewage sludge waste [52,53].

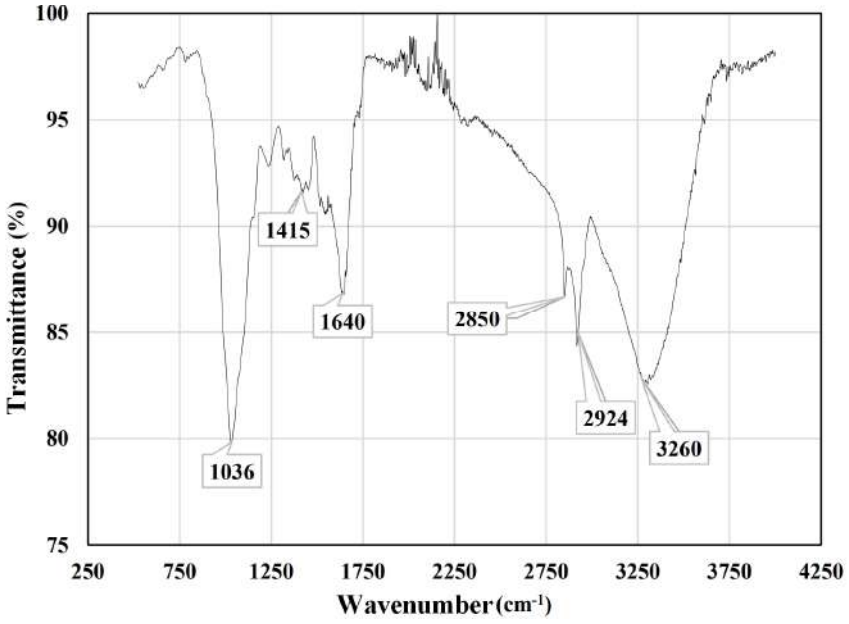

Figure 4. FTIR spectrum of the biomass.

The calorific value of the biomass was determined as 3674 cal/g. XRF analysis was performed on the ash obtained from the biomass, and the elemental composition is presented in Table 1. An additional XRF analysis conducted on the sample prior to combustion in the muffle furnace revealed similar mineral constituents, along with an SO_3 content of 6.40%.

Table 1. XRF analysis of the biomass ash.

Content	SiO_2	Fe_2O_3	CaO	SrO	P_2O_5	MnO	BaO	NiO	TiO_2	K_2O	Cr_2O_3	CuO	V_2O_5	Ln_2O_3
%	34.34	11.58	26.50	0.59	8.10	0.85	0.23	0.24	0.71	14.14	0.34	0.32	0.05	1.70

3.2. Leaching Experiments

The following sections examine the effects of the key leaching parameters to clarify their contribution to the dissolution mechanism.

3.2.1. Effect of Solid to Liquid Ratio

Examination of Figure 5a shows that increasing the solid-to-liquid ratio diminishes the influence of acid concentration and reduces the dissolution of all elements. At constant solution volume and acid concentration, a higher solid loading lowers the amount of acid available per particle, thereby decreasing overall leaching efficiency. Consequently, to achieve maximum manganese dissolution in the presence of HNO_3, a solid concentration of 100 g L^{-1} was selected as the fixed parameter for subsequent experiments. Since the dissolution remained low at this stage, the XRD patterns in Figure 5b show no significant changes.

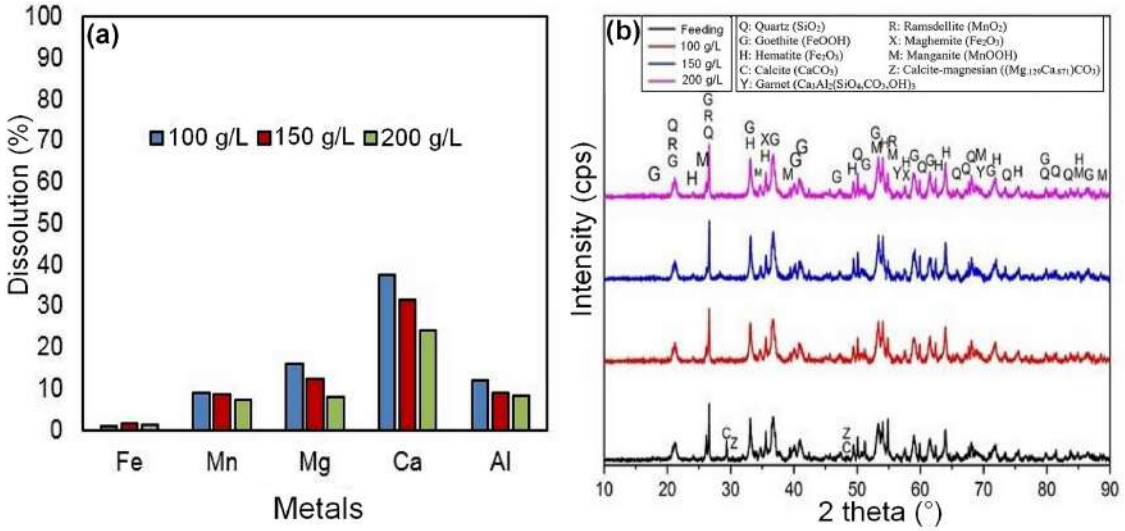

Figure 5. Elemental dissolution as a function of varying solid–liquid ratios at 70 °C, 1 h leaching time, 300 rpm stirring speed, and 1 M HNO_3 (**a**), and corresponding XRD patterns of the leach residues (**b**).

3.2.2. Effect of Acid Concentration

The dissolution behaviour of Fe, Mn, Mg, Ca, and Al as a function of HNO_3 concentration at different temperatures is presented in Figure 6. Increasing the acid concentration generally enhanced the leaching of all elements, although the extent of dissolution varied significantly among them. Calcium exhibited the highest sensitivity to acid concentration, with its dissolution exceeding 80% at concentrations ≥4 M, particularly at elevated temperatures. In contrast, Mn dissolution remained relatively limited at room temperature

and 50 °C, where the maximum leaching did not exceed 10%. A marked increase in Mn recovery was observed only under more aggressive leaching conditions (≥70 °C and ≥4 M HNO_3), reaching a maximum dissolution of approximately 33% at 90 °C and 5 M HNO_3. These results indicate that while acid concentration plays a critical role in facilitating the dissolution of Ca, its influence on Mn and other elements is considerably less pronounced under mild leaching conditions. To establish a systematic workflow, temperature and HNO_3 concentration were first optimized (Figure 6), followed by evaluation of organic reductants under the selected conditions and kinetic studies for selected reductant systems.

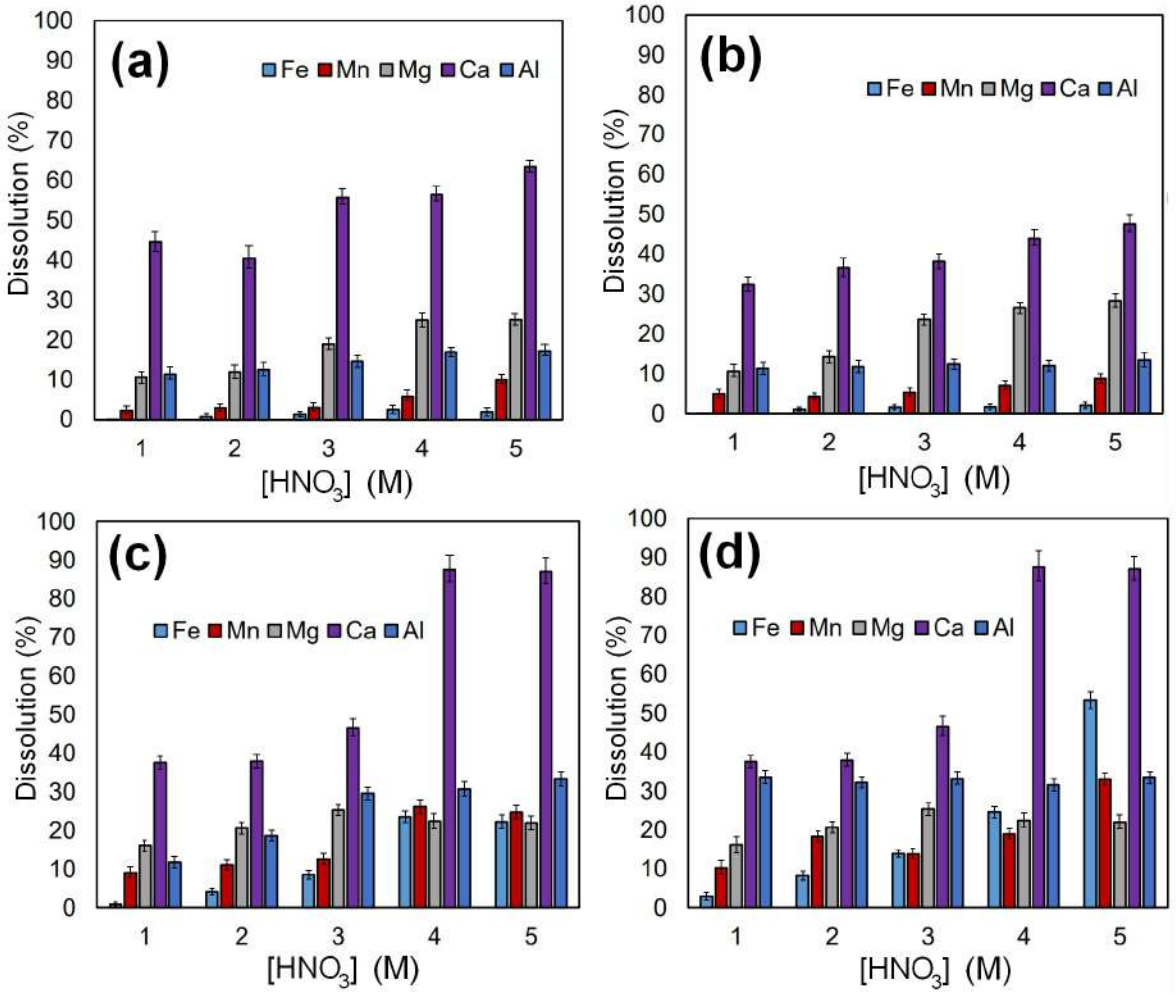

Figure 6. Dissolution behavior of Fe, Mn, Mg, Ca, and Al at different HNO_3 concentrations and temperatures under the conditions of 300 rpm stirring speed, 100 g/L solid-to-liquid ratio, and 1 h reaction time: (**a**) 25 °C, (**b**) 50 °C, (**c**) 70 °C, and (**d**) 90 °C.

3.2.3. Effect of Temperature

The influence of temperature on the leaching behaviour is also evident in Figure 6, where dissolution efficiencies consistently improved with increasing reaction temperature. At higher temperatures (≥70 °C), the leaching of Mn, Fe, and Mg increased notably, although still remaining moderate compared to Ca. The strong dependence of Ca dissolution on both temperature and acid concentration suggests the preferential breakdown of calcite phases under such conditions. This interpretation is further supported by the XRD patterns in Figure 7, where the characteristic calcite peaks show a marked reduction

in intensity and, in some cases, near disappearance, indicating that the calcite phase has largely dissolved with increasing acid concentration and temperature. Similarly, peaks corresponding to Mn-bearing phases diminished significantly at ≥70 °C, confirming the partial dissolution of manganese minerals under harsher leaching environments. Overall, the combined dissolution data and XRD results clearly demonstrate that temperature is a decisive factor in promoting mineral breakdown and enhancing metal recovery, particularly for Mn at high acid concentrations.

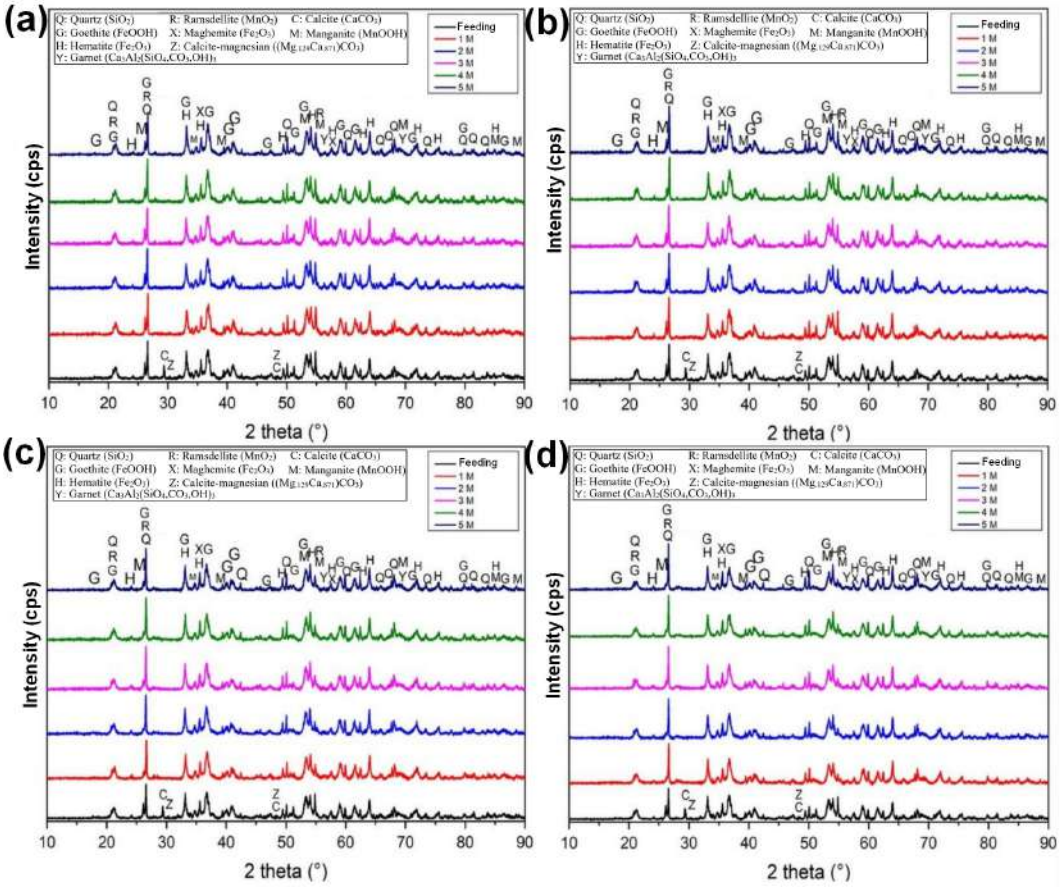

Figure 7. XRD patterns of the leach residues obtained at different HNO_3 concentrations and temperatures under the conditions of 300 rpm stirring speed, 100 g/L solid-to-liquid ratio, and 1 h reaction time: (**a**) 25 °C, (**b**) 50 °C, (**c**) 70 °C, and (**d**) 90 °C.

Since the selective dissolution of manganese while retaining iron in the leach solution was desired, the conditions of 1 M HNO_3 concentration, 70 °C reaction temperature, 300 rpm stirring speed, 100 g/L solid-to-liquid ratio, and 1 h reaction time were identified as the optimum parameters. These conditions were subsequently employed in the following experiments.

3.2.4. Effect of Reductants

The influence of different reductants on the leaching performance of manganese and iron in the presence of HNO_3 is illustrated in Figure 8. Among the tested organic reductants, oxalic, citric, and tartaric acids exhibited the most pronounced effects. The maximum Mn dissolution yield was approximately 60% in the presence of oxalic acid (Figure 8a), while citric acid addition at 30 g/L slightly enhanced the Mn dissolution to about 65%

(Figure 8b). Tartaric acid demonstrated a comparable performance, with dissolution values close to those obtained with oxalic and citric acids (Figure 8c). In contrast, maleic acid yielded considerably lower Mn dissolution efficiencies, around 40% at 30 g/L (Figure 8d).

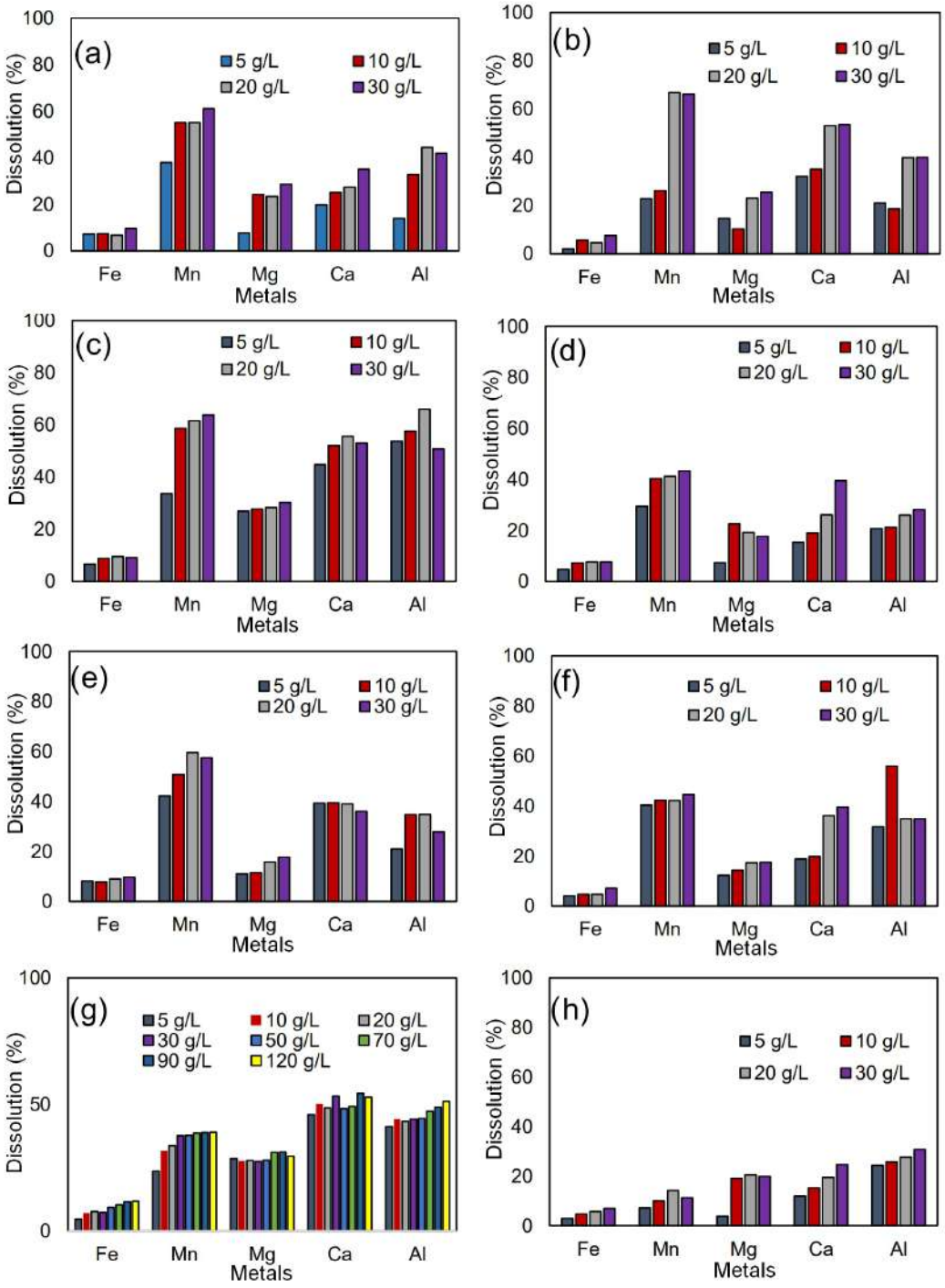

Figure 8. Effect of different reductants on the dissolution behaviour of manganese and iron under leaching conditions of 1 M HNO_3, 70 °C, 300 rpm stirring speed, 100 g/L pulp density, and 1 h reaction time: (**a**) oxalic acid, (**b**) citric acid, (**c**) tartaric acid, (**d**) maleic acid, (**e**) glucose, (**f**) sucrose, (**g**) biomass (horse dung), and (**h**) acetic acid.

Glucose addition significantly improved Mn dissolution, achieving values of approximately 60% at 20 g/L (Figure 8e), while sucrose led to dissolution yields ranging between 40% and 44% depending on concentration (Figure 8f). In the case of biomass, reductant addition was increased up to 120 g/L in order to enhance dissolution. However, only marginal differences in Mn recovery were observed between 30 g/L and 120 g/L, with dissolution values consistently ranging between 40% and 45%. The reductive capacity of the biomass arises from its intrinsic organic constituents and the low-molecular-weight organic acids formed during degradation, as supported by FTIR data and prior HPLC results [38] (Figure 8g). The use of acetic acid did not result in any noticeable improvement in Mn dissolution efficiency (Figure 8h). Across all reductants, Fe dissolution remained below 10%, confirming the high selectivity of the process. The overall order of element dissolution under reductive leaching conditions was Mn > Ca > Al > Mg > Fe. The XRD patterns of the leach residues in Figure 9 corroborate the dissolution data. The intensity of diffraction peaks corresponding to manganese-bearing phases such as manganite and ramsdellite decreased progressively with the addition of reductants, consistent with the higher Mn dissolution observed. Furthermore, an increase in quartz peak intensity was identified with increasing reductant concentrations, except in the case of biomass, where such changes were not detected. This suggests a preferential dissolution of manganese phases over silicate phases, in line with the trends noted in the leaching results. When comparing the relative effectiveness of reductants at the lowest concentrations tested, their performance in enhancing Mn dissolution followed the order: glucose > sucrose > oxalic acid > tartaric acid > maleic acid > biomass > citric acid > acetic acid. At the highest concentrations, however, the ranking shifted, with citric acid becoming the most effective, followed by tartaric acid > oxalic acid > glucose > sucrose > maleic acid > biomass > acetic acid. At low reductant concentrations, the dissolution behaviour is primarily governed by the intrinsic reducing strength of the organic species, resulting in higher effectiveness for simple sugars such as glucose and sucrose. As the reductant concentration increases, however, polycarboxylic acids such as citric and tartaric acid begin to dominate due to their stronger complexation ability, which enhances Mn^{2+} stabilization and promotes continued dissolution. This concentration-dependent shift reflects a transition from a reduction-controlled regime to one in which ligand complexation and metal–organic speciation become increasingly influential. These results highlight the significant dependence of reductive leaching efficiency not only on the type of reductant employed but also on its dosage, underlining the complex interaction between organic reductants and the Mn-bearing mineral phases during acid leaching. The differences in dissolution efficiency among the reductants arise from their molecular structures and intrinsic redox behavior. Polycarboxylic acids such as tartaric and citric acid contain multiple –COOH and –OH groups that enhance electron donation and facilitate the reduction of Mn(IV/III) to Mn(II). In contrast, sugars generate less stable intermediate radicals, and biomass or acetic acid contains fewer active functional groups, resulting in lower Mn dissolution. This structure-dependent trend aligns with the dissolution behavior observed in this study.

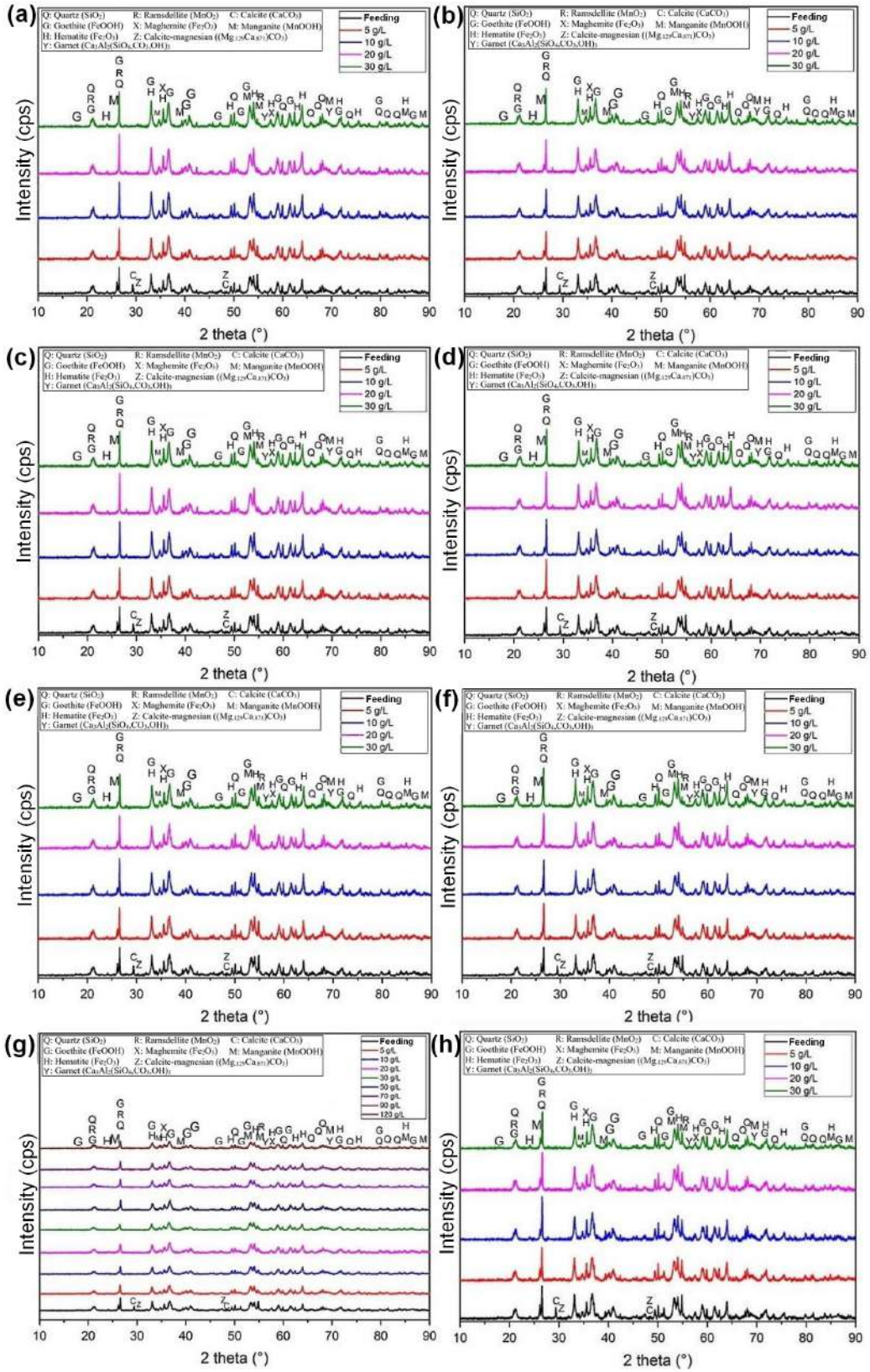

Figure 9. XRD patterns of the undissolved solids obtained after leaching in 1 M HNO_3 solution at 70 °C, with a solid-to-liquid ratio of 100 g/L, stirring rate of 300 rpm, and leaching time of 1 h under different reductant additions: (**a**) oxalic acid, (**b**) citric acid, (**c**) tartaric acid, (**d**) maleic acid, (**e**) glucose, (**f**) sucrose, (**g**) biomass, and (**h**) acetic acid.

https://doi.org/10.3390/min16010047

In addition to the enhanced dissolution of Mn under reductive conditions, the consistently low dissolution of Fe (<10%) can be explained by the distinct electrochemical stability of iron in nitric acid media. Under the strongly acidic and oxidizing environment of 1 M HNO_3, iron remains thermodynamically stabilized in the Fe^{3+} state, and the reduction of Fe^{3+} to Fe^{2+} requires redox potentials significantly lower than those attainable with the organic reductants employed here. Thus, while reductants readily convert Mn(IV/III) phases to soluble Mn^{2+}, they are not thermodynamically capable of reducing Fe^{3+}. Moreover, Fe-oxide phases such as hematite and goethite exhibit inherently slow dissolution kinetics in nitrate media and may form thin Fe(III)-oxyhydroxide layers that act as transient passivating films. These combined thermodynamic and kinetic factors explain why Fe dissolution remains limited even under conditions that strongly promote Mn leaching, thereby underpinning the high selectivity observed in this study.

3.2.5. Kinetic Studies

At this stage, the dissolution mechanisms of Mn were investigated in experiments employing tartaric acid and biomass as reductants, which constitutes the novel aspect of this study since such reductants have not previously been applied for Fe–Mn ores in the presence of HNO_3. Dissolution data were obtained at different temperatures and leaching times, and the Mn dissolution rates were analysed to determine their conformity with various reaction order kinetic models. Once the reaction orders were identified, rate constants were employed to construct Arrhenius plots, as expressed in the following equation:

$$k = Ae^{\frac{-Ea}{RT}} \quad (3)$$

where k is the rate constant (min^{-1}), T is the absolute temperature (K), Ea is the activation energy (kJ mol^{-1}), R is the universal constant (8314 J mol^{-1} K^{-1}), and A is the pre-exponential factor.

The dissolution kinetics of Mn in HNO_3 medium were further examined using the shrinking core model, and the results were evaluated through Equations (4) and (5). Subsequently, the rate constants were applied to derive the Arrhenius plots, from which the activation energies were calculated.

$$1 - (1 - \alpha)^{\frac{1}{3}} = k \times t \quad (4)$$

$$1 - 2(1 - \alpha)^{\frac{1}{3}} + (1 - \alpha)^{\frac{2}{3}} = k \times t \quad (5)$$

where k is the rate constant (min^{-1}), α is the conversion or dissolution fraction determined between 0 and 1, and t is leaching time (min).

The dissolution kinetics of Mn were investigated under controlled leaching conditions using two novel reductants: biomass (horse dung) and tartaric acid, in the presence of HNO_3. The experiments were performed at a stirring rate of 300 rpm, with 1 M HNO_3 concentration, a pulp density of 100 g/L, and reductant dosages of 120 g/L biomass or 30 g/L tartaric acid, respectively. Leaching tests were carried out at four different temperatures (30, 50, 70, and 90 °C) and varying leaching times up to 3 h. The results for biomass and tartaric acid are presented in Figure 10 and Figure 11, respectively. For the biomass-assisted system (Figure 10a–d), the dissolution of Mn increased significantly with both temperature and leaching time, while Fe dissolution remained consistently low across all conditions, confirming the reductive selectivity of biomass toward Mn. At 90 °C, nearly complete Mn dissolution (>90%) was achieved within 3 h, whereas at lower temperatures (30–50 °C) dissolution remained moderate. Similar trends were observed for other associated elements (Mg, Ca, Al), though their dissolution ratios were markedly lower com-

pared to Mn, highlighting the preferential leaching of manganese. The corresponding kinetic plots (Figure 10e) demonstrated good linearity when fitted with the shrinking core model based on Equation (5), indicating that Mn dissolution is controlled predominantly by chemical reaction at the surface rather than by diffusion. The Arrhenius plot (Figure 10f) yielded an apparent activation energy (Ea) of 27.74 kJ·mol^{-1}, suggesting that the process lies at the boundary between diffusion- and reaction-controlled regimes but is more consistent with a chemically controlled reaction mechanism.

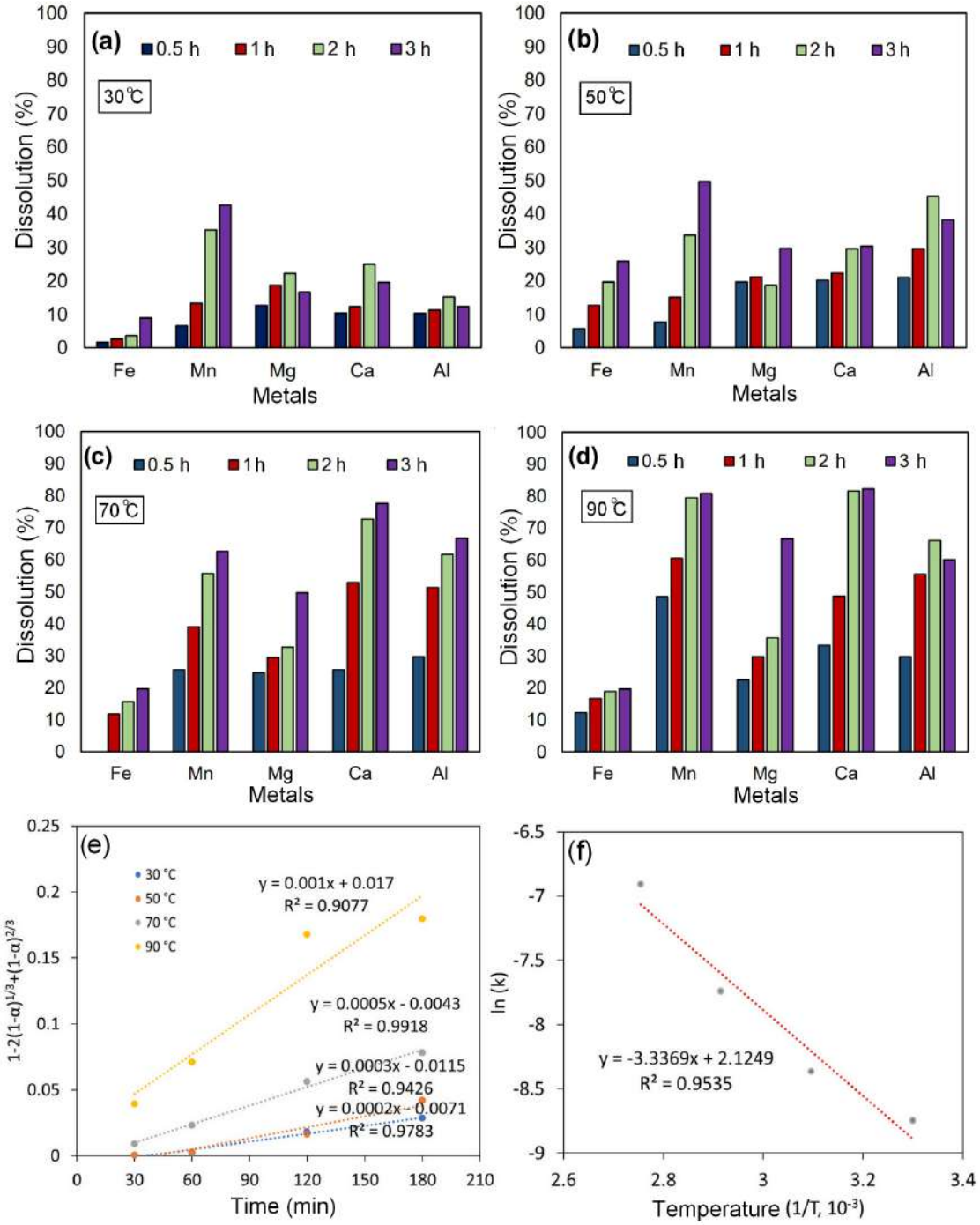

Figure 10. Dissolution of Fe, Mn, Mg, Ca, and Al in 1 M HNO_3 with 120 g/L biomass reductant (100 g/L pulp density, 300 rpm) at 30–90 °C and varying times (**a**–**d**), with kinetic (**e**) and Arrhenius (**f**) plots.

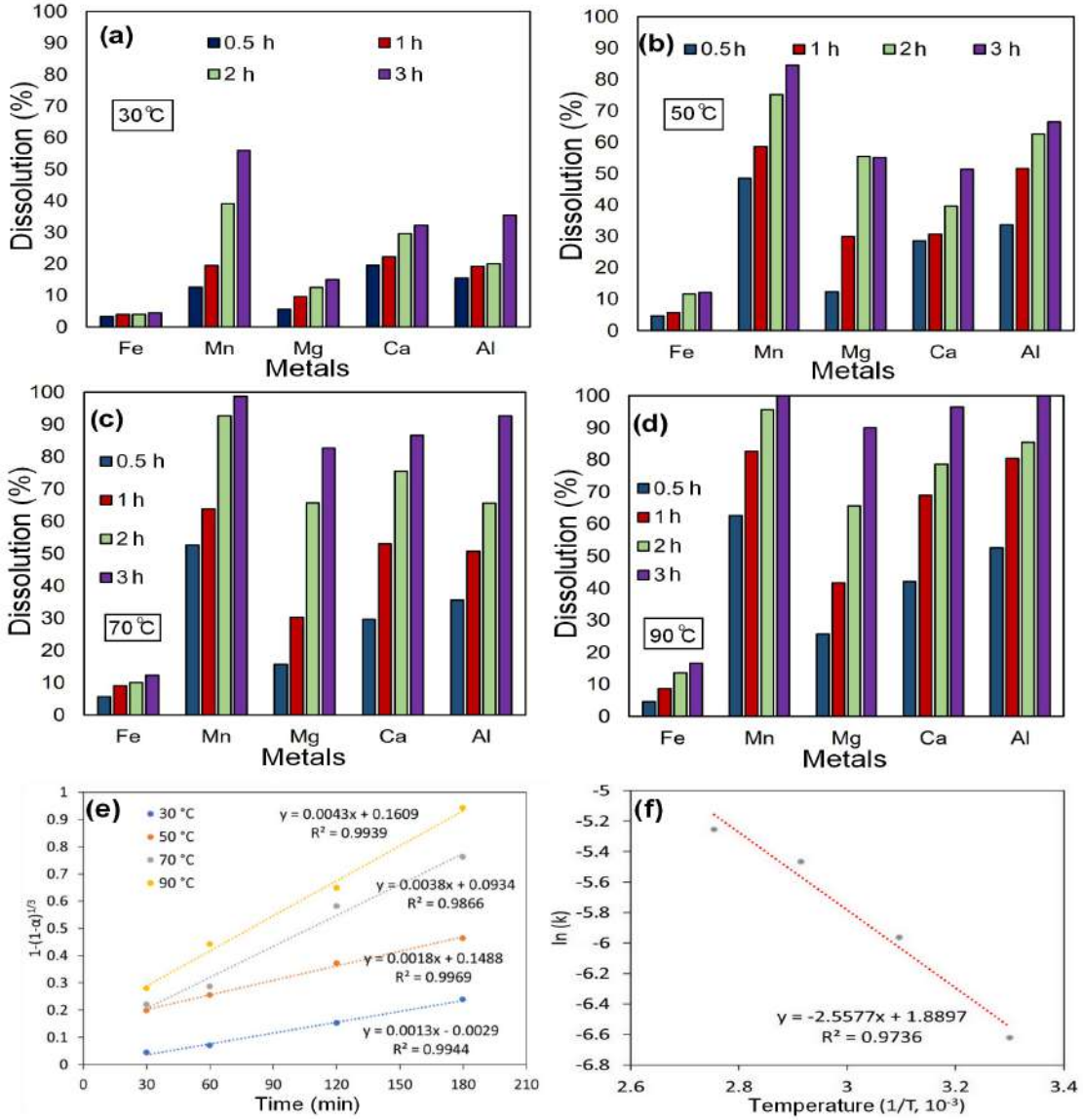

Figure 11. Dissolution of Fe, Mn, Mg, Ca, and Al in 1 M HNO_3 with 30 g/L tartaric acid reductant (100 g/L pulp density, 300 rpm) at 30–90 °C and varying times (**a**–**d**), with kinetic (**e**) and Arrhenius (**f**) plots.

In the case of tartaric acid as the reductant (Figure 11a–d), a similar temperature and time dependence of Mn dissolution was observed, with markedly enhanced extraction efficiency compared to biomass at lower temperatures. At 70–90 °C, Mn dissolution exceeded 80%–90%, whereas at 30 °C, values remained below 40%. The dissolution of Fe was again suppressed under all conditions, ensuring selective Mn recovery. The kinetic fits (Figure 11e) showed strong agreement with the shrinking core model given by Equation (6), implying that the dissolution process may involve a combination of surface chemical reaction and diffusion through a product layer. The corresponding Arrhenius plot (Figure 11f) provided an activation energy of 21.26 kJ·mol^{-1}, slightly lower than that for the biomass system, suggesting a comparatively lower energy barrier and higher efficiency for tartaric acid in promoting Mn dissolution. It should be noted that the activation energies were determined under the optimal reductant dosages for each system, and

therefore, they reflect mechanistic differences rather than a direct comparison at equivalent concentrations. The activation energies obtained in this study, namely 27.74 kJ·mol^{-1} for the biomass system and 21.26 kJ·mol^{-1} for the tartaric acid system, fall within the range typically associated with surface-controlled reductive dissolution in nitric acid in the presence of organic reductants. A very similar activation energy of approximately 25.7 kJ·mol^{-1} was reported by Lasheen et al. [42] for the reductive leaching of manganese using molasses in nitric acid. This close agreement in activation energy indicates that the dissolution process is governed by energetically accessible surface-controlled reactions, facilitated by organic electron donors during the reduction of higher-valence manganese species to Mn^{2+}. Although activation energies were not reported, two additional studies employing organic reductants in nitric acid [41,43] also demonstrated effective manganese dissolution, and their findings further support the conclusion that organic reductants promote surface electron-transfer processes that are consistent with the activation energies determined in the present work. Overall, the results clearly indicate that both biomass and tartaric acid act as effective reductants in the nitric acid medium, enabling the selective dissolution of Mn over Fe. However, tartaric acid appears to be kinetically more favourable, as reflected by its lower activation energy and better performance at lower temperatures. The application of such reductants for Fe–Mn ores in HNO_3 medium has not previously been reported, highlighting the novelty of this work. The kinetic analysis confirms that the dissolution of Mn follows the shrinking core model, with activation energies consistent with chemically controlled leaching processes. These findings provide valuable insights for the design of energy-efficient and selective hydrometallurgical processes for manganese recovery from complex Fe–Mn ores.

4. Conclusions

The present study provides a systematic investigation of manganese dissolution from a complex manganiferous iron ore using nitric acid as the leaching medium in combination with organic reductants. The results clearly demonstrate that HNO_3 alone was insufficient to achieve significant Mn recovery under mild conditions; however, the introduction of suitable reductants markedly improved leaching efficiency. Among the eight reductants tested, tartaric acid and biomass from horse dung exhibited the most promising behaviour and were selected for detailed kinetic evaluation. Under the optimized leaching conditions of 1 M HNO_3, 100 g/L pulp density, 300 rpm stirring speed, and 30–90 °C, Mn dissolution increased substantially with temperature and reaction time, while Fe dissolution consistently remained below 10%. The maximum Mn extraction exceeded 90% at 90 °C with biomass addition and reached nearly 85%–90% with tartaric acid at elevated temperatures, indicating the high selectivity of both reductants in suppressing Fe solubilisation. These results confirm the effectiveness of organic reductants in achieving targeted Mn recovery from Fe–Mn ores. Kinetic studies revealed that the dissolution data were well described by the shrinking core model. For the biomass system, the dissolution behaviour was best explained by the surface chemical reaction model, yielding an apparent activation energy of 27.74 kJ/mol. In contrast, tartaric acid followed a mixed mechanism involving surface reaction and diffusion through the product layer, with a lower activation energy of 21.26 kJ/mol. The relatively small values of Ea obtained in both cases suggest that Mn dissolution in nitric acid medium proceeds with moderate energy requirements, highlighting the energy-efficient nature of the process. These findings contribute to the broader development of environmentally sustainable hydrometallurgical approaches for the valorisation of complex Fe–Mn ores, offering an alternative pathway for Mn recovery that minimizes Fe contamination and reduces chemical costs.

Author Contributions: S.T.: Conceptualization, Methodology, Data curation, Investigation, Writing—original draft, Writing—review & editing, Funding; M.A.: Methodology, Experimental work, Investigation, Writing—review & editing; H.V.: Methodology, Investigation, Writing—review & editing; S.K.: Methodology, Experimental work, Investigation, Writing—review & editing; S.S.: Conceptualization, Methodology, Data curation, Writing—original draft, Writing—review & editing, Funding, Visualisation. All authors have read and agreed to the published version of the manuscript.

Funding: This study was financially supported by the Scientific and Technological Research Council of Turkey (TÜBİTAK) under Project No. 119M690.

Data Availability Statement: Data is contained within the article.

Conflicts of Interest: The authors declare no competing interests.

References

1. Ji, G.; Gao, X.; Sohn, I.; Ueda, S.; Wang, W. Review of beneficiation techniques and new thinking for comprehensive utilization of high-phosphorus iron ores. *Miner. Eng.* **2025**, *223*, 109176. https://doi.org/10.1016/j.mineng.2025.109176.
2. Sahu, S.N.; Behera, P.; Sahoo, S.; Sushobhan, B.R. A Critical Review on the Magnetization Roasting of Low/Lean-Grade Iron Ore Resources Using Renewable/Non-Renewable Reductant: An Approach Towards Iron ore Sustainability. *J. Sustain. Metall.* **2025**, *11*, 160–185. https://doi.org/10.1007/s40831-024-01001-2.
3. Li, X.; Li, X.; Ma, X.; Li, C.; Cai, H.; Zhong, H.; Wang, S. Sustainable high-purity $MnSO_4 \cdot H_2O$ preparation for $LiMn_2O_4$ production: Utilizing low-grade manganese carbonate ore via solvent extraction without saponification. *Sep. Purif. Technol.* **2025**, *380*, 135270. https://doi.org/10.1016/j.seppur.2025.135270.
4. Holley, E.A.; Fahle, L.; Smith, N.M.; Deberdt, R.; Calderon, J.; Gibbs, G.; Bazilian, M. Graphite and manganese mining in the U.S.: Proposed projects and federal battery mineral policies. *Resour. Policy* **2025**, *108*, 105689. https://doi.org/10.1016/j.resourpol.2025.105689.
5. Sokolova, I.; Nwaila, G.T.; Ntunka, M.G.; Klochkov, S.; Michaux, S.; Moscardini, E.; Toro, L.; Ghorbani, Y. From abundant resource to critical commodity: Forecasting manganese supply and assessing its sustainability. *Sustain. Mater. Technol.* **2025**, *44*, e01349. https://doi.org/10.1016/j.susmat.2025.e01349.
6. Huang, S.; Fu, Y. Enrichment Characteristics and Mechanisms of Critical Metals in Marine Fe-Mn Crusts and Nodules: A Review. *Minerals* **2023**, *13*, 1532. https://doi.org/10.3390/min13121532.
7. Konhauser, K.O.; Planavsky, N.J.; Hardisty, D.S.; Robbins, L.J.; Warchola, T.J.; Haugaard, R.; Lalonde, S.V.; Partin, C.A.; Oonk, P.B.H.; Tsikos, H.; et al. Iron formations: A global record of Neoarchaean to Palaeoproterozoic environmental history. *Earth-Sci. Rev.* **2017**, *172*, 140–177. https://doi.org/10.1016/j.earscirev.2017.06.012.
8. Cannon, W.F.; Kimball, B.E.; Corathers, L.A. Manganese. In *Critical Mineral Resources of the United States—Economic and Environmental Geology and Prospects for Future Supply*; Schulz, K.J., DeYoung, J.H., Jr., Seal, R.R., II, Bradley, D.C., Eds.; U.S. Geological Survey Professional Paper 1802; U.S. Geological Survey: Reston, VA, USA, 2017; pp. L1–L28. https://doi.org/10.3133/pp1802L.
9. Arachchige, L.J.; Li, C.; Wang, F. Recent advances in understanding iron/steel corrosion: Mechanistic insights from molecular simulations. *Curr. Opin. Solid State Mater. Sci.* **2025**, *35*, 101216. https://doi.org/10.1016/j.cossms.2025.101216.
10. Gramlich, A.; Helbig, C.; Schmidt, M.; Hagedorn, W. A comprehensive design approach to increase the performance of steels under minimal costs and environmental impacts. *Sustain. Mater. Technol.* **2024**, *41*, e01040. https://doi.org/10.1016/j.susmat.2024.e01040.
11. Zhang, X.; Niu, Z.; Zhang, Q.; Yuanxing, Y.; Gao, P.; Han, Y. Efficient development of ultra-low-grade iron ore by hydrogen-based mineral phase transformation: Magnetic transition, phase transformation, and microstructure evolution. *Int. J. Hydrogen Energy* **2025**, *97*, 757–765. https://doi.org/10.1016/j.ijhydene.2024.11.469.
12. Sun, X.; Liu, G.; Liang, X.; Tong, S. Superior Comprehensive Mechanical Properties of a Low-Carbon Medium Manganese Steel for Replacing AISI 4330 Steel in the Oil and Gas Industry. *Materials* **2023**, *16*, 490. https://doi.org/10.3390/ma16020490.
13. Marinova, D.; Kalapsazova, M.; Zlatanova, Z.; Mereacre, L.; Zhecheva, E.; Stoyanova, R. Lithium Manganese Sulfates as a New Class of Supercapattery Materials at Elevated Temperatures. *Materials* **2023**, *16*, 4798. https://doi.org/10.3390/ma16134798.
14. Singh, V.; Chakraborty, T.; Tripathy, S.K. A Review of Low Grade Manganese Ore Upgradation Processes. *Miner. Process. Extr. Metall. Rev.* **2019**, *41*, 417–438. https://doi.org/10.1080/08827508.2019.1634567.

15. Xiong, D.; Lu, L.; Holmes, R.J. Chapter 9—Physical separation of iron ore: Magnetic separation. In *Iron Ore*, 2nd ed.; Lu, L., Ed.; Woodhead Publishing: Cambridge, UK, 2022; pp. 309–332. https://doi.org/10.1016/B978-0-12-820226-5.00010-0.
16. Kosdauletov, N.; Nurumgaliyev, A.; Zhautikov, B.; Suleimen, B.; Adilov, G.; Kelamanov, B.; Smirnov, K.; Zhuniskaliyev, T.; Kuatbay, Y.; Bulekova, G.; et al. Selective Reduction of Iron from Iron–Manganese Ore of the Keregetas Deposit Using Hydrogen. *Metals* **2025**, *15*, 691. https://doi.org/10.3390/met15070691.
17. Pourbaix, M. *Atlas of Electrochemical Equilibria in Aqueous Solutions*; Pergamon Press: Oxford, UK, 1974.
18. Sobianowska-Turek, A.; Szczepaniak, W.; Zabłocka-Malicka, M. Electrochemical evaluation of manganese reducers—Recovery of Mn from Zn–Mn and Zn–C battery waste. *J. Power Sources* **2014**, *270*, 668–674. https://doi.org/10.1016/j.jpowsour.2014.07.136.
19. Veglio, F.; Toro, L. Fractional factorial experiments in the development of manganese dioxide leaching by sucrose in sulphuric acid solutions. *Hydrometallurgy* **1994**, *36*, 215–230. https://doi.org/10.1016/0304-386X(94)90007-8.
20. Nayak, B.B.; Mishra, K.G.; Paramguru, R.K. Kinetics and mechanism of MnO_2 dissolution in H_2SO_4 in the presence of pyrite. *J. Appl. Electrochem.* **1999**, *29*, 191–200. https://doi.org/10.1023/A:1003490810114.
21. Momade, F.; Momade, Z. Reductive Leaching of Manganese Oxide Ore İn Aqueous Methanol–Sulphuric Acid Medium. *Hydrometallurgy* **1999**, *51*, 103–113. https://doi.org/10.1016/S0304-386X(98)00077-2.
22. Naik, P.K.; Sukla, L.B.; Das, S.C. Aqueous SO_2 leaching studies on Nishikhal manganese ore through factorial experiment. *Hydrometallurgy* **2000**, *54*, 217–228. https://doi.org/10.1016/S0304-386X(99)00075-4.
23. Sahoo, R.N.; Naik, P.K.; Das, S.C. Leaching of manganese from low-grade manganese ore using oxalic acid as reductant ın sulphuric acid solution. *Hydrometallurgy* **2001**, *62*, 157–163. https://doi.org/10.1016/S0304-386X(01)00196-7.
24. Hariprasad, D.; Dash, B.; Ghosh, M.K.; Anand, S. Leaching of manganese ores using sawdust as a reductant. *Miner. Eng.* **2007**, *20*, 1293–1295. https://doi.org/10.1016/j.mineng.2007.07.013.
25. Cheng, Z.; Zhu, G.; Zhao, Y. Study in reduction-roast leaching manganese from low-grade manganese dioxide ores using cornstalk as reductant. *Hydrometallurgy* **2009**, *96*, 176–179. https://doi.org/10.1016/j.hydromet.2008.08.004.
26. Lasheen, T.A.; El-Hazek, M.N.; Helal, A.S.; El-Nagar, W. Recovery of manganese using molasses as reductant ın nitric acid solution. *Int. J. Miner. Process.* **2009**, *92*, 109–114. https://doi.org/10.1016/j.minpro.2009.03.001.
27. Wang, Y.; Jin, S.; Lv, Y. Hydrometallurgical process and kinetics of leaching manganese from semioxidized manganese ores with sucrose. *Minerals* **2017**, *7*, 27–40. https://doi.org/10.3390/min7020027.
28. Muthalib, N.; Abdullah, N.S.; Ismail, S. Reductive Leaching of Low Grade Manganese Ore (LGMO) Using Glucose in Sulphuric Acid: Optimization Condition Using Response Surface Methodology. *ASEAN Eng. J.* **2018**, *8*, 64–73. https://doi.org/10.11113/aej.v8.15503.
29. Tian, X.; Wen, X.; Yang, C.; Liang, Y.; Pi, Z.; Wang, Y. Reductive leaching of manganese from low-grade manganese oxide ores using corncob as reductant ın sulfuric acid solution. *Hydrometallurgy* **2010**, *100*, 157–160. https://doi.org/10.1016/j.hydromet.2009.11.008.
30. Nayl, A.A.; Ismail, I.M.; Aly, H.F. Recovery of pure $MnSO_4{\cdot}H_2O$ by reductive leaching of manganese from pyrolusite ore by sulfuric acid and hydrogen peroxide. *Int. J. Miner. Process.* **2011**, *100*, 116–123. https://doi.org/10.1016/j.minpro.2011.05.003.
31. Tang, Q.; Zhong, H.; Wang, S.; Li, J.; Liu, G. Reductive leaching of manganese oxide ores using waste tea as reductant ın sulfuric acid solution. *Trans. Nonferrous Met. Soc. China* **2014**, *24*, 861–867. https://doi.org/10.1016/S1003-6326(14)63136-8.
32. Li, C.; Zhong, H.; Wang, S.; Xue, J.; Wu, F.; Zhang, Z. Manganese extraction by reduction–acid leaching from low-grade manganese oxide ores using cas as reductant. *Trans. Nonferrous Met. Soc. China* **2015**, *25*, 1677–1684. https://doi.org/10.1016/S1003-6326(15)63772-4.
33. Lu, Y.; Ma, H.; Huang, R.; Yuan, A.; Huang, Z.; Zhou, Z. Reductive leaching of low-grade pyrolusite with formic acid. *Metall. Mater. Trans. B* **2015**, *46*, 1709–1715. https://doi.org/10.1007/s11663-015-0380-4.
34. Xiong, S.; Li, X.; Liu, P.; Hao, S.; Hao, F.; Yin, Z.; Liu, J. Recovery of manganese from low-grade pyrolusite ore by reductively acid leaching process using lignin as a low cost reductant. *Miner. Eng.* **2018**, *125*, 126–132. https://doi.org/10.1016/j.mineng.2018.06.003.
35. Prasetyo, E.; Purwaningsih, E.; Astuti, W. Selective-reductive leaching of manganese from lowgrade manganese ore using tannic acid as reductant. *Min. Metall. Explor.* **2019**, *36*, 1003–1012. https://doi.org/10.1007/s42461-019-00115-6.
36. Sinha, M.K.; Purcell, W.; Van Der Westhuizen, W.A. Recovery of manganese from ferruginous manganese ore using ascorbic acid as reducing agent. *Miner. Eng.* **2020**, *154*, 106406. https://doi.org/10.1016/j.mineng.2020.106406.
37. Muthalib, N.; Ismail, S.; Abdullah, N.S.; Jabit, N.A. Reductive leaching of low-grade manganese ore with bamboo sawdust: Study of bamboo sawdust and glucose degradation. *Arab. J. Chem.* **2021**, *14*, 103288. https://doi.org/10.1016/j.arabjc.2021.103288.

38. Top, S.; Altiner, M.; Kursunoglu, S. Separation of Mn and Fe from a Manganiferous Iron Ore Using Horse Dung as Reductant: A Zero Waste Approach. *JOM* **2022**, *74*, 474–483. https://doi.org/10.1007/s11837-021-05057-3.
39. Sultana, N.; Al-Amin, K.; Alahi, F.; Jahan, N.; Ferdous, J.; Gafur, M.A. Extraction of copper from printed circuit board (PCB) in nitric and sulphuric acid media through pyrolysis and incineration. *Next Sustain.* **2025**, *6*, 100223. https://doi.org/10.1016/j.nxsust.2025.100223.
40. Rozalen, M.; Huertas, F.J. Comparative effect of chrysotile leaching in nitric, sulfuric and oxalic acids at room temperature. *Chem. Geol.* **2013**, *352*, 134–142. https://doi.org/10.1016/j.chemgeo.2013.06.004.
41. Pagnanelli, F.; Furlani, G.; Valentini, P.; Vegliò, F.; Toro, L. Leaching of low-grade manganese ores by using nitric acid and glucose: Optimization of the operating conditions. *Hydrometallurgy* **2004**, *75*, 157–167. https://doi.org/10.1016/j.hydromet.2004.07.007.
42. Lasheen, T.A.; El Hazek, M.N.; Helal, A.S. Kinetics of reductive leaching of manganese oxide ore with molasses in nitric acid solution. *Hydrometallurgy* **2009**, *98*, 314–317. https://doi.org/10.1016/j.hydromet.2009.05.006.
43. Ologwu, C.A.; Nwankwo, J.I.; Chinyelu, C.E.; Akuchie, J.C. Enhancing the Efficiency of Manganese Recovery from Pyrolusite Ore through Hydrometallurgical Techniques Utilizing Nitric Acid and Distilled Water. *Int. J. Innov. Sci. Res. Technol.* **2023**, *8*, 1055–1067.
44. Altiner, M.; Top, S.; Bouchekrit, C.; Kursunoglu, S. Production of Mn_3O_4 nanoparticles from a manganiferous iron ore via reductive leaching, precipitation, and calcination. *Hydrometallurgy* **2022**, *208*, 105810. https://doi.org/10.1016/j.hydromet.2021.105810.
45. Oguzberk, C. *Adana Ceyhan Dokuz Tekne Köyü Manganez Zuhuru Raporu (Manganese Occurrence Report in Adana Ceyhan Dokuz Tekne Village)*; MTA Press: Ankara, Turkey, 1975. Available online: https://eticaret.mta.gov.tr/index.php?route=product/product&product_id=19196 (accessed on 10 December 2025).
46. Öztürk, H. Manganese deposits in Turkey: Distribution, types and tectonic setting. *Ore Geol. Rev.* **1997**, *12*, 187–203. https://doi.org/10.1016/S0169-1368(97)00005-X.
47. Lu, X.; Wang, J.; Al-Qadiri, H.M.; Ross, C.F.; Powers, J.R.; Tang, J.; Rasco, B.A. Determination of total phenolic content and antioxidant capacity of onion (*Allium cepa*) and shallot (*Allium oschaninii*) using infrared spectroscopy. *Food Chem.* **2011**, *129*, 637–644. https://doi.org/10.1016/j.foodchem.2011.04.105.
48. Guerrero, P.; Garrido, T.; Leceta, I.; De La Caba, K. Films based on proteins and polysaccharides: Preparation and physical-chemical characterization. *Eur. Polym. J.* **2013**, *49*, 3713–3721. https://doi.org/10.1016/j.eurpolymj.2013.08.014.
49. Silva, S.D.; Feliciano, R.P.; Boas, L.V.; Bronze, M.R. Application of FTIR-ATR to Moscatel dessert wines for prediction of total phenolic and flavonoid contents and antioxidant capacity. *Food Chem.* **2014**, *150*, 489–493. https://doi.org/10.1016/j.foodchem.2013.11.028.
50. Singh, R.K.; Kukrety, A.; Sharma, O.P.; Baranwal, S.; Atray, N.; Ray, S.S. Study of a novel phenolic-ester as antioxidant additive in lube, biodiesel and blended diesel. *J. Ind. Eng. Chem.* **2016**, *37*, 27–31. https://doi.org/10.1016/j.jiec.2016.03.029.
51. Demir, P.; Onde, S.; Severcan, F. Phylogeny of cultivated and wild wheat species using ATR-FTIR spectroscopy. *Spectrochim. Acta Part A Mol. Biomol. Spectrosc.* **2015**, *135*, 757–763. https://doi.org/10.1016/j.saa.2014.07.025.
52. Grube, M.; Lin, J.G.; Lee, P.H.; Kokorevicha, S. Evaluation of sewage sludge-based compost by FT-IR spectroscopy. *Geoderma* **2006**, *130*, 324–333. https://doi.org/10.1016/j.geoderma.2005.02.005.
53. Baharuddin, A.S.; Rahman, N.A.A.; Shah, U.K.M.; Hassan, M.A.; Wakisaka, M.; Shirai, Y. Evaluation of pressed shredded empty fruit bunch (EFB)-palm oil mill effluent (POME) anaerobic sludge based compost using Fourier transform infrared (FTIR) and nuclear magnetic resonance (NMR) analysis. *Afr. J. Biotechnol.* **2011**, *10*, 8082–8089. https://doi.org/10.5897/AJB10.548.